Radiation Physics and Chemistry 167 (2020) 108273

Contents lists available at ScienceDirect

Radiation Physics and Chemistry

journal homepage: www.elsevier.com/locate/radphyschem

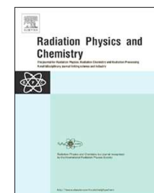

Intrinsic spatial resolution limit of the analyzer-based X-ray phase contrast imaging technique

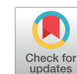

Marcelo G. Hönnicke[a,*], Sérgio L. Morelhão[b]

[a] Universidade Federal da Integração Latino-Americana, 85867-970, Foz do Iguaçu, PR, Brazil
[b] Instituto de Física, Universidade de São Paulo, 05508-090, São Paulo, SP, Brazil

ARTICLE INFO

Keywords:
Phase-contrast X-ray imaging
Extinction depth blur
Intrinsic spatial resolution

ABSTRACT

Dynamical diffraction effects always play a role when working with perfect single crystals. The penetration of X-rays respect to the surface normal during diffraction (extinction depth - $1/\sigma_e$) in perfect single crystals does not have a constant value. The value changes for different angular positions on the crystal diffraction condition. For higher X-ray energies this value can change from few micrometers to tens of millimeters for each different crystal angular position in the small angular range of the diffraction condition. This effect may spread a single point in the object (sample) as a line in the image detector, especially if the crystal is set (or if the sample angularly deviates the beam) at lower diffraction angle positions, where the surface component of X-ray penetration can achieve huge values. Then, for imaging experiments where the dynamical diffraction occurs, such intrinsic property can affect the image resolution. We have modeled and experimentally checked such a dynamical diffraction property using, as example, an Analyzer-based X-ray phase contrast imaging setup (ABI) at two different X-ray energies: 10.7 keV and 18 keV. The results show that our theoretical model is consistent with the measured results. For higher energies the blur effect is enhanced and intrinsically limits the image spatial resolution.

1. Introduction

Dynamical diffraction effects always play a role when working with perfect and nearly perfect single crystals (strained due to stress crystals). Within the dynamical condition, the penetration of X-rays respect to the surface normal during diffraction (extinction depth) in perfect single crystals does not have a constant value (Pinsker, 1978; Authier, 2001; Hönnicke and Cusatis, 2005; Hönnicke et al., 2008a). The value changes for different angular positions on the crystal diffraction condition. For higher X-ray energies this value can change from few micrometers to tens of millimeters for each different crystal angular position in the small angular range of the diffraction condition (Hönnicke et al., 2008a). Such an effect can be minimized for nearly perfect single crystals, since the strain due to stress, strongly affects the extinction (Authier, 2001; Tanner, 1976).

Then, for imaging experiments, when dynamical diffraction occurs (Davis et al., 1995; Morelhao et al., 2010; Zhou et al., 2014; Caudevilla et al., 2017; Ludwig et al., 2001; Johnson et al., 2008; Shabalin et al., 2017; Hu et al., 2018), the variable extinction depth may spread a single point in the object (sample) as a line in the image detector. This spoils the image resolution especially if the crystal (or portion of the sample) is set (or it is) at the lower diffraction angle position on its diffraction profile (rocking curve), where the surface component of X-ray extinction can achieve huge values. Note that, very often, in imaging experiments when dynamical diffraction occurs, the extinction depth is considered, theoretically, to have a constant value since the major part of the works take use of the extinction length (or Pendellösung length) (Λ_B) which presents a constant value (Hu et al., 2018; Kaganer et al., 2001; Nesterets et al., 2004).

In this work, the variable extinction depth effect is theoretically and experimentally explored, using as an example, an analyzer-based X-ray phase contrast imaging setup (ABI) (Hönnicke et al., 2007, 2008b) in Bragg case (Fig. 1) with symmetrically-cut perfect single crystals at two different X-ray energies (10.7 keV and 18 keV). Theoretical studies were modeled by simulating the ABI images of a 300 µm polyamide wire. Two different approaches were employed in the simulations: (i) analyzer crystal for a plane and monochromatic X-ray wave beam and; (ii) non-dispersive double crystal setup. For the modelling validation, the simulated images were compared with measured ones taken from a real 300 µm polyamide wire. It is good to mention here, that quantitative analyzer based X-ray phase contrast imaging have been widely explored in the literature (Kaganer et al., 2001; Nesterets et al., 2004; Davies, 1996; Kitchen et al., 2007; Bravin et al., 2007; Maksimenko, 2007; Zhang et al., 2007; Hönnicke et al., 2012; Majidi et al., 2014) and

* Corresponding author.
E-mail address: marcelo.honnicke@unila.edu.br (M.G. Hönnicke).

https://doi.org/10.1016/j.radphyschem.2019.04.023
Received 15 December 2018; Received in revised form 12 April 2019; Accepted 13 April 2019
Available online 22 April 2019
0969-806X/ © 2019 Elsevier Ltd. All rights reserved.

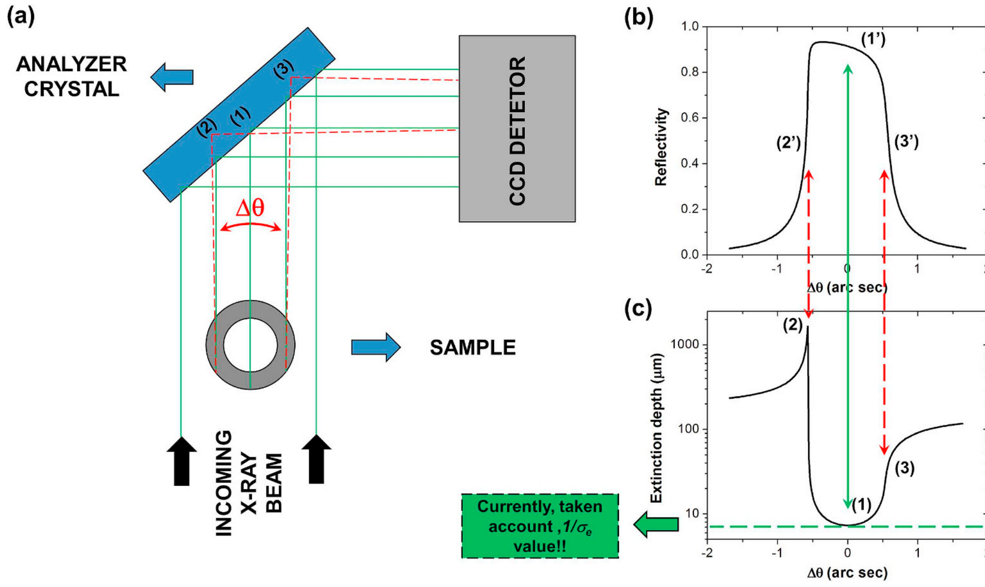

Fig. 1. (a) Schematic representation of an analyzer-based X-ray phase contrast imaging (ABI) for a plane and monochromatic wave beam. The sample slightly deviates, angularly (Δθ), the portion of the X-ray beam which cross the sample. Such deviation can be seen as an angular scan of the beam by the analyzer crystal. As an example, only three different positions (1–3) are represented in the figure. In our model to simulate the images, around 30 different positions were considered (corresponding to 30 different spatial positions on the portion of the beam cross section which crosses the sample). (b) The portion of the X-ray beam which cross the sample angularly scan the analyzer crystal as a rocking curve where, as an example, only three different angular positions are shown (1′-3′) The different angular positions correspond to different extinction depth ($1/\sigma_e$) on the analyzer crystal (1–3) (c). The variable extinction depth is responsible for changing (blurring) the projected image.

where, when mentioned, the extinction depth is based on the extinction length (Kaganer et al., 2001; Nesterets et al., 2004) which is considered to have a constant value.

2. Dynamical diffraction and extinction depth

For determining the X-ray penetration in single crystals in (extinction depth) and out (penetration depth) of the diffraction condition, we need to explore the Dynamical Theory of X-ray diffraction for plane and monochromatic X-ray wave beam approximation. Then, the penetration depth ($1/\sigma$) can be defined as (Pinsker, 1978):

$$\frac{1}{\sigma} = \frac{\gamma_0}{\mu} \tag{1}$$

where σ is the attenuation factor μ is the linear attenuation coefficient and γ_0 is the direction cosine of the incident angle respect to the crystal surface normal.

For the extinction depth ($1/\sigma_e$), where σ_e is the extinction factor, for easy representation of the equations, we firstly define the y scale (angularly dependent):

$$y = \frac{-\chi_0 + \left(1 - \frac{|\chi_0|}{2}\right).\,(\theta - \theta_0).\,\sin(2\theta)}{C.\,|\chi_h|} \tag{2}$$

where χ_0 and χ_h.are the polarizabilities, θ_0 is the diffraction angle, θ is the Bragg angle and C is the polarization factor. In the y scale, the angular range where the diffraction occurs, is divided in three different regions: $y > 1$ (I) (maximum wavefield amplitude on the atomic planes), $1 > y > -1$ (II) (maximum reflectivity region) and $y < -1$ (III) (maximum wavefield amplitude between the atomic planes). Then, the extinction depth ($1/\sigma_e$), for the adjacent regions of the maximum reflectivity (I and III), will be given by:

$$\frac{1}{\sigma_e^{I,III}} = \frac{\gamma_0}{\mu\left|\left[\frac{y-\varepsilon}{\sqrt{y^2-1}}\right]\right|} \tag{3}$$

where ε is the dielectric constant. And, for the maximum reflectivity region the extinction depth ($1/\sigma_e$) is given by:

$$\frac{1}{\sigma_e^{II}} = \frac{\gamma_0}{\mu\left|\left[\frac{C|\chi_{hr}|}{|\chi_{0i}|}\sqrt{1-y^2}\left(1 + \frac{b^2}{8(1-y^2)}\right)\right]\right|} \tag{4}$$

where χ_{hr}.and χ_{0i}.are the real and imaginary parts of the polarizabilities χ_h.and χ_0, respectively. At last, the extinction depth ($1/\sigma_e$) for $y = \pm 1$ is given by:

$$\frac{1}{\sigma_e^{\pm 1}} = \frac{\gamma_0}{\mu\sqrt{C\frac{|\chi_{hr}|}{|\chi_{0i}|}[1 \mp \varepsilon]}} \tag{5}$$

With the equations from (2) to (5) one can plot the extinction deph *versus* angle as shown in Fig. 1c). Note that, the extinction depth limit ($1/\sigma_e$) for large $|y|$ is the penetration depth ($1/\sigma$). Also, as mentioned in the introduction, very often, for imaging experiments when dynamical diffraction occurs, the extinction depth, based on the extinction length (Hu et al., 2018; Kaganer et al., 2001; Nesterets et al., 2004), is considered, theoretically, to have a constant value, so that:

$$\frac{1}{\sigma_e^{cons\tan t}} = \frac{\Lambda_B}{\gamma_0} \tag{6}$$

If one takes $y = 0$ in equation (4), we should get, approximately, the same value got with equation (6) as, schematically shown by, the green dashed line in Fig. 1c).

3. Modelling the simulated images

We have worked with two different approaches. Firstly, we created scripts, which works in Matlab or Octave, to simulate the expected acquired images with a plane and monochromatic X-ray wave beam. Secondly, an improved model, based on a non-dispersive double crystal setup was created, based on scripts which also works in Matlab or Octave, to compare with experimental results. Both models were created for a Bragg case ABI for two different setups: Si 333 crystals at 10.7 keV and Si 444 crystals at 18 keV.

3.1. Plane and monochromatic X-ray wave beam

For this approach we firstly simulated the extinction depth and the Darwin-Prins curve of Si 333 at 10.7 keV and Si 444 at 18 keV for symmetric Bragg case. The simulated curves for Si 333 at 10.7 keV is shown in Fig. 1b and c. These curves were stored in the database. After that, we have simulated the angular deviations of the X-ray beam, including the X-ray beam attenuation, for a 300 μm polyamide wire. This simulation was done with a resolution of 10 μm, i.e., the portion of the beam cross section which cross the sample was striped in 30 different sections. Since each sample strip is characterized by one angular deviation ($\Delta\theta$) of the beam and, each angular deviation can be seen as an

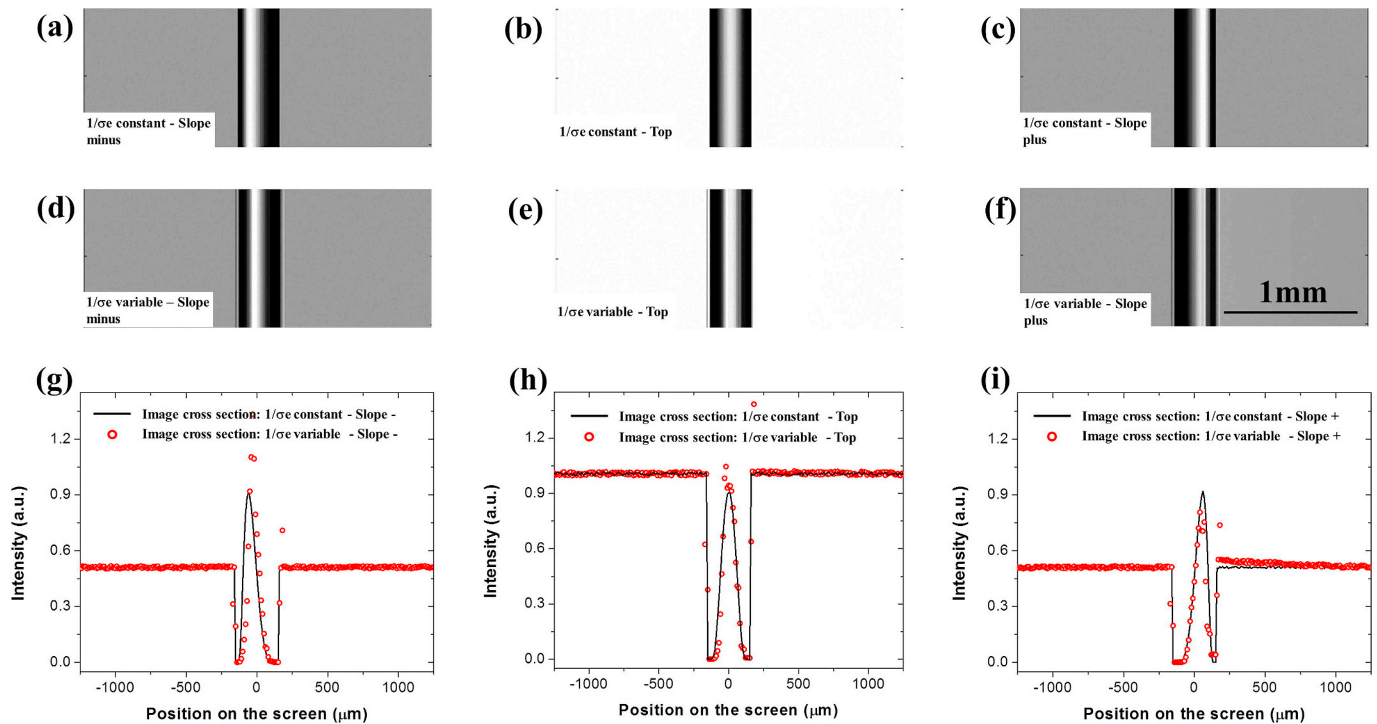

Fig. 2. Simulated analyzer-based X-ray phase contrast images (ABI) of a 300 μm thick polyamide wire, for a plane and monochromatic X-ray wave beam and Si 333 analyzer crystal at 10.7 keV. (a–c) Slope minus, top and slope plus images for $1/\sigma_e$ constant. (d–f) Slope minus, top and slope plus images for $1/\sigma_e$ variable. (g–i) Image cross sections. Solid black lines: $1/\sigma_e$ constant. Open red circles: $1/\sigma_e$ variable. (For interpretation of the references to colour in this figure legend, the reader is referred to the Web version of this article.)

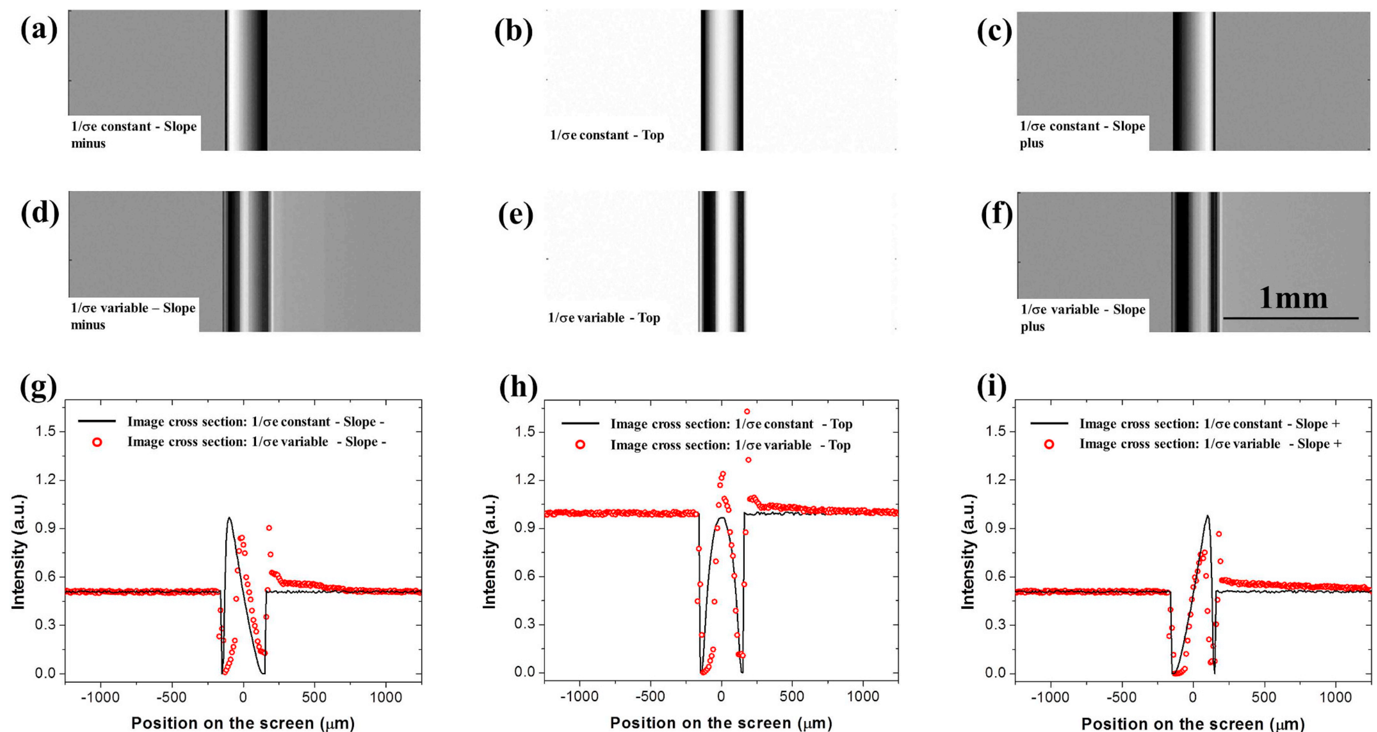

Fig. 3. Simulated analyzer-based X-ray phase contrast imaging (ABI) of a 300 μm thick polyamide wire, for a plane and monochromatic X-ray wave beam and Si 444 analyzer crystal at 18 keV. (a–c) Slope minus, top and slope plus images for $1/\sigma_e$ constant. (d–f) Slope minus, top and slope plus images for $1/\sigma_e$ variable. (g–i) Image cross sections. Solid black lines: $1/\sigma_e$ constant. Open red circles: $1/\sigma_e$ variable. (For interpretation of the references to colour in this figure legend, the reader is referred to the Web version of this article.)

angular scan of the beam by the analyzer crystal, the angular deviations for each different sample strip was stored in the database and then matched with the correspondent extinction depth and the correspondent reflectivity values. Then, a reflectivity value and an extinction depth value are attributed to each sample strip. The intensity registered in a two dimensional detector, for each sample strip, is then

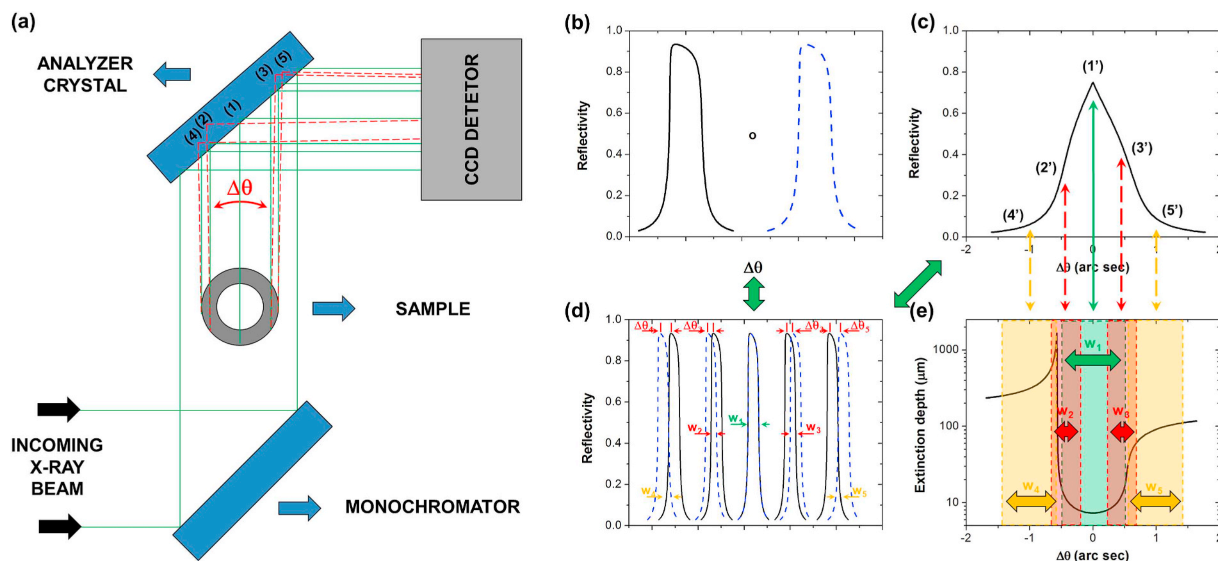

Fig. 4. (a) Schematic representation of an analyzer-based X-ray phase contrast imaging (ABI) for a non-dispersive double crystal setup. As mentioned in Fig. 1, the sample slightly deviates, angularly (Δθ), the portion of the X-ray beam which crosses the sample. Such deviation can be seen as an angular scan of the beam by the analyzer crystal. As an example, only five different positions (1–5) are represented in the figure. In our model to simulate the images, around 30 different positions were considered (corresponding to 30 different spatial positions on the portion of the beam cross section which cross the sample). (b) For non-dispersive double crystal, the portion of the beam which is angularly deviated by the sample, and angularly scan this beam portion in the analyzer crystal, can be represented by a correlation of the Darwin-Prins curve of the monochromator (first crystal) and the Darwin-Prins curve of the analyzer (second crystal) which results in a diffraction profile (rocking curve) shown in (c) where, as an example, five different angular positions (1′-5′) are shown. (d) Schematic representation of the correlation process. For each different angular deviation (defined by different Δθs), a different angular width (w_1 to w_5) is restricted by the two crystals. The different widths are used to average (Gaussian normalized) the different extinction depths ($1/\sigma_e$), schematically shown, by the different angular stripes in (d).

spread in different areas corresponding to different $(1/\sigma_e)\gamma_0$ (Fig. 1a). The intensity in each area is normalized by the maximum reflectivity value of each sample strip. Also the spread beam has an exponential decay over its cross section for each sample strip. This information is stored in a single image matrix and summed up for each one of the image strip. The final image results joined with their cross sections are shown in Fig. 2 for Si 333 at 10.7 keV and in Fig. 3 for Si 444 at 18 keV for three different angular positions on the analyzer crystal (slope minus, top and slope plus, which correspond to positions 2, 1 and 3, respectively in Fig. 1a). The results are compared with simulated images taken for constant $(1/\sigma_e)$ values. Strong differences were detected for both cases. However, these simulations are for an ideal case (plane and monochromatic X-ray wave beam). To be more realists we carried on a similar approach for a non-dispersive double crystal setup for symmetric Bragg case which is very often used for ABI purposes.

3.2. Non-dispersive double crystal setup

This setup is used for analyzer-based X-ray phase contrast imaging. The setup modeled here (Fig. 4) is for a Bragg case and symmetrically-cut crystals. For this approach we firstly had to simulate the analyzer rocking curve (Fig. 4c), which now is a correlation between the Darwin-Prins curve of the first crystal (monochromator) and the Darwin-Prins curve of the second crystal (analyzer) (Fig. 4b and d). The correlated reflectivity curves of Si 333 at 10.7 keV and Si 444 at 18 keV for symmetric Bragg case were stored in the database. For the extinction depth values since each sample strip is characterized by one angular deviation ($\Delta\theta$) of the beam and, each angular deviation can be seen as an angular scan of the beam by the analyzer crystal, we can look for the schematic representation of the correlation procedure (Fig. 4d) and consider that, for each angular deviation there is a range of $1/\sigma_e$ limited by the width (w) (Fig. 4e). This gets the $1/\sigma_e$ profile smoother. Such an average procedure was modulated by a Gaussian profile. Then, the averaged $1/\sigma_e$ values for each angular deviation (or sample strip) was also stored in the database. Again, we have simulated the angular deviations of the X-ray beam, including the X-ray beam attenuation, for a 300 μm polyamide wire with the same parameters described in the previous sub-section. The stored angular deviations for each different sample strip are then matched with the correspondent averaged $1/\sigma_e$ and the correspondent correlated reflectivity values. Again, a reflectivity value and an extinction depth value are attributed to each sample strip. The intensity registered in a two dimensional detector, for each sample strip, is then spread in different areas corresponding to different averaged $(1/\sigma_e)$. γ_0 (Fig. 4a). The intensity in each area is normalized by the maximum correlated reflectivity value of each sample strip. As in the previous subsection, the spread beam has an exponential decay over its cross section for each sample strip. This information is stored in a single image matrix and summed up for each one of the image strip. The final image results joined with their cross sections are shown in Fig. 5 for Si 333 at 10.7 keV and in Fig. 6 for Si 444 at 18 keV for three different angular positions on the analyzer crystal (slope minus, top and slope plus, which correspond to positions 2, 1 and 3, respectively in Fig. 4a). The results are compared with simulated images taken for constant $(1/\sigma_e)$ values. For lower energies (10.7 keV) no differences could be seen. Differences were detected only for the higher energies (18 keV). We can still try to estimate the blurring as function of energy. This is an estimative, since the blur depends, among other factors, of $(1/\sigma_e)\gamma_0$ and of the rocking curve width, which changes from one diffraction plane to other, even for the same X-ray energy. The changes in both quantities strongly affect the blur sensitivity. Then, we simulated another set of ABIs for an X-ray beam energy of 14 keV with a non-dispersive double crystal Si 333 setup. Therefore, we have simulated ABIs at three different energies in order to estimate, in a graph, the contribution to the blurring as function of the X-ray beam energy. To do the graphics, first we need to quantify the blurring. For that we defined the Relative Image Blur (RIB) as:

$$RIB = \frac{\left(dI/dx\right)_{1/\sigma_e-\text{variable}}}{\left(dI/dx\right)_{1/\sigma_e-cons\tan t}} \tag{7}$$

where $(dI/dx)_{1/\sigma e\ -variable}$ is the derivative of the intensity respect to the

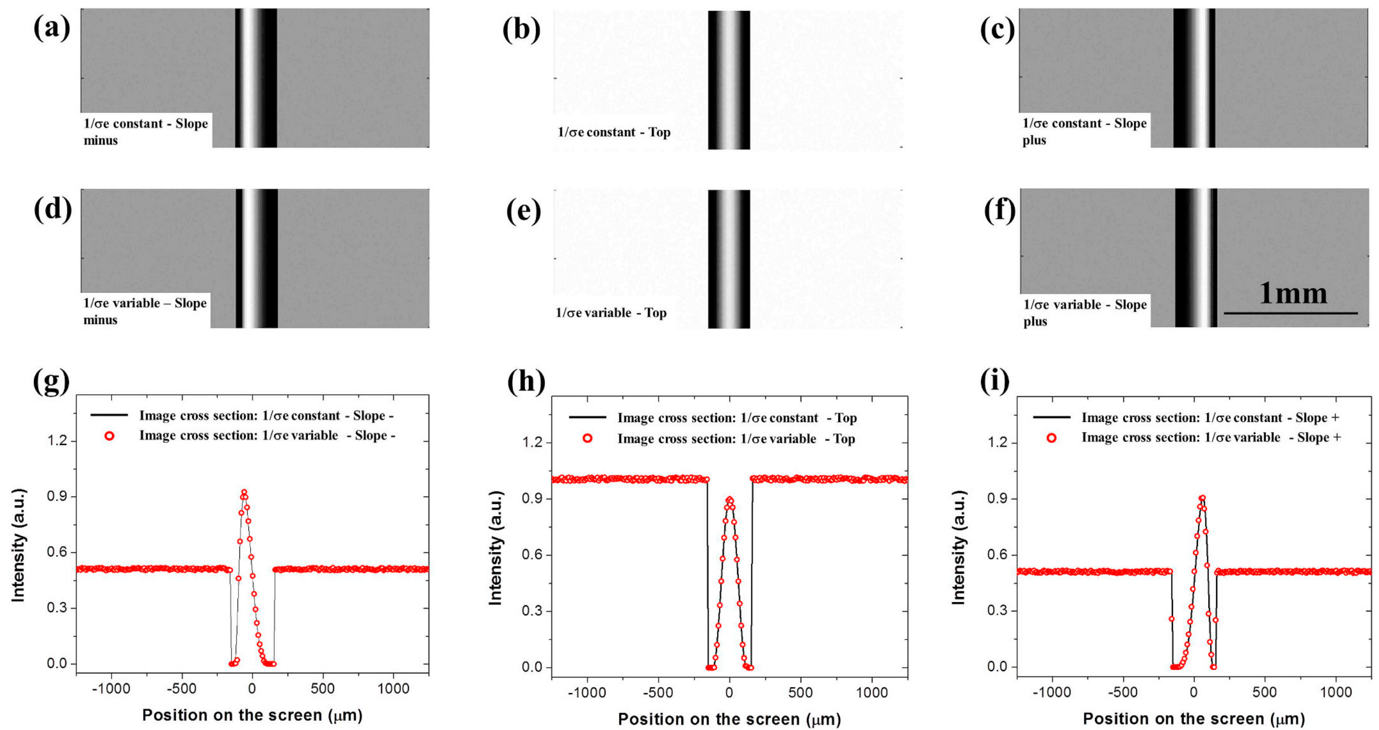

Fig. 5. Simulated analyzer-based X-ray phase contrast images (ABI) of a 300 μm thick polyamide wire, for a non-dispersive double crystal setup and Si 333 analyzer crystal at 10.7 keV. (a–c) Slope minus, top and slope plus images for $1/\sigma_e$ constant. (d–f) Slope minus, top and slope plus images for $1/\sigma_e$ variable. (g–i) Image cross sections. Solid black lines: $1/\sigma_e$ constant. Open red circles: $1/\sigma_e$ variable. For this approach at lower X-ray energies (10.7 keV) any difference was detected among constant and variable $1/\sigma_e$. (For interpretation of the references to colour in this figure legend, the reader is referred to the Web version of this article.)

position on the area detector across the sample edge for variable $1/\sigma_e$ ABIs and $(dI/dx)_{1/\sigma e\ -constant}$ is the derivative of the intensity respect to the position on the area detector across the sample edge for constant $1/\sigma_e$ ABIs. The RIB results are shown in Fig. 7 for ABIs simulated at the three different angular positions on the analyzer crystal (slope minus, top and slope plus, which correspond to positions 2, 1 and 3,

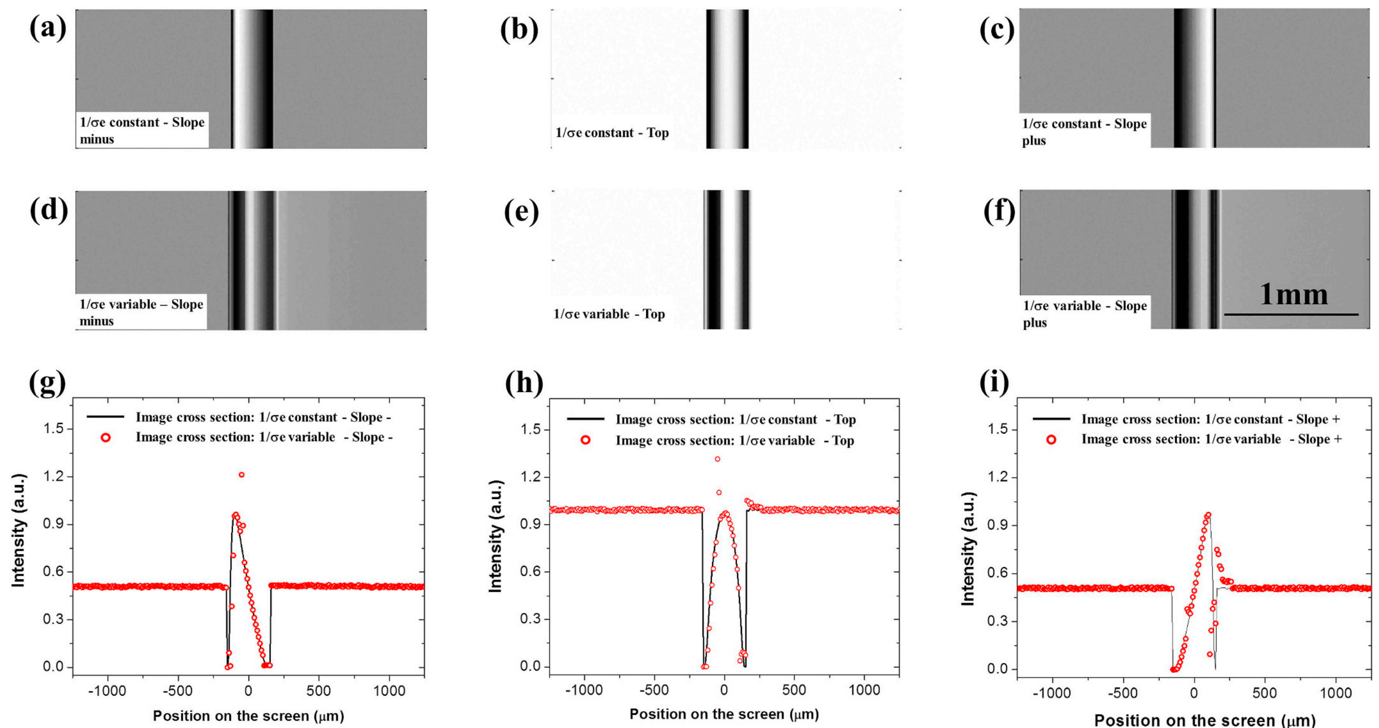

Fig. 6. Simulated analyzer-based X-ray phase contrast images (ABI) of a 300 μm thick polyamide wire, for a non-dispersive double crystal setup and Si 444 analyzer crystal at 18 keV. (a–c) Slope minus, top and slope plus images for $1/\sigma_e$ constant. (d–f) Slope minus, top and slope plus images for $1/\sigma_e$ variable. (g–i) Image cross sections. Solid black lines: $1/\sigma_e$ constant. Open red circles: $1/\sigma_e$ variable. For this approach at higher X-ray energies (18 keV) differences were detected among constant and variable $1/\sigma_e$. (For interpretation of the references to colour in this figure legend, the reader is referred to the Web version of this article.)

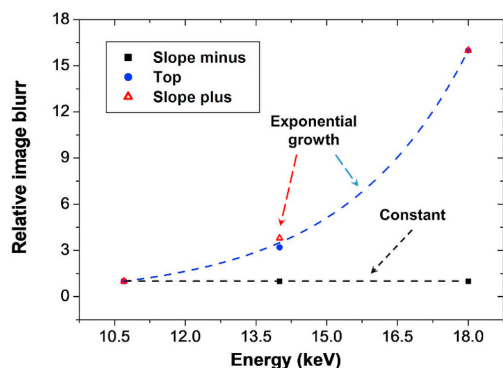

Fig. 7. Relative image blur (RIB) versus X-ray beam energy calculated from the acquired simulated images for the non-dispersive double crystal setup for three different X-ray beam energies (10.7 keV and Si 333,14 keV and Si 333 and 18 keV and Si444) and three different angular positions on the analyzer crystal (slope minus, top and slope plus, which correspond to positions 2, 1 and 3, respectively in Fig. 4a). The RIB was determined across the left sample edge.

respectively in Fig. 4a). For the top and slope minus angular positions there is a tendency to an exponential growth of RIB. However, as previously mentioned, this is an estimative. More exhaustive simulations on different diffraction planes and diffraction plane orders at different X-ray beam energies need to be carried out in order to predict such RIB behaviour.

At last, to check the validity of our theoretical model we compared it with experimental results which will be described in the next section.

4. Experimental validation

For the experimental validation of our theoretical model (blur due to the dynamical diffraction condition), we have taken experimental images of a 300 μm polyamide wire, acquired with two different ABI non-dispersive setups (Si 333 double crystal setup at 10.7 keV and Si 444 double crystal setup at 18 keV), described elsewhere (Hönnicke et al., 2007, 2008b). However, since the detectors are different in both experimental cases, we had to include in our Matlab/Octave scripts the image detector contribution (blur due to the image detector instrumentation).

For the 10.7 keV ABI setup a direct conversion CCD detector with pixel size of $22.5 \times 22.5\,\mu m^2$ was employed. Since the theoretical pixel size of our theoretical model is $10 \times 10\,\mu m^2$, we included an average 2×2 binning in our final simulated image. The simulated image results including the detector contribution and the measured images joined with their image cross sections are shown in Fig. 8 for two different angular positions on the analyzer crystal (top and slope plus, which correspond to positions 1 and 3, respectively in Fig. 4a).

For the 18 keV ABI setup, an indirect conversion CCD detector with pixel size of $3.5 \times 3.5\,\mu m^2$ and a 2×2 binning was employed. The calculated spatial resolution of this detector with the 2×2 binning is $24 \times 24\,\mu m^2$. This was included in our simulated images with a point spread function (PSF) of 24 μm. The simulated image results including

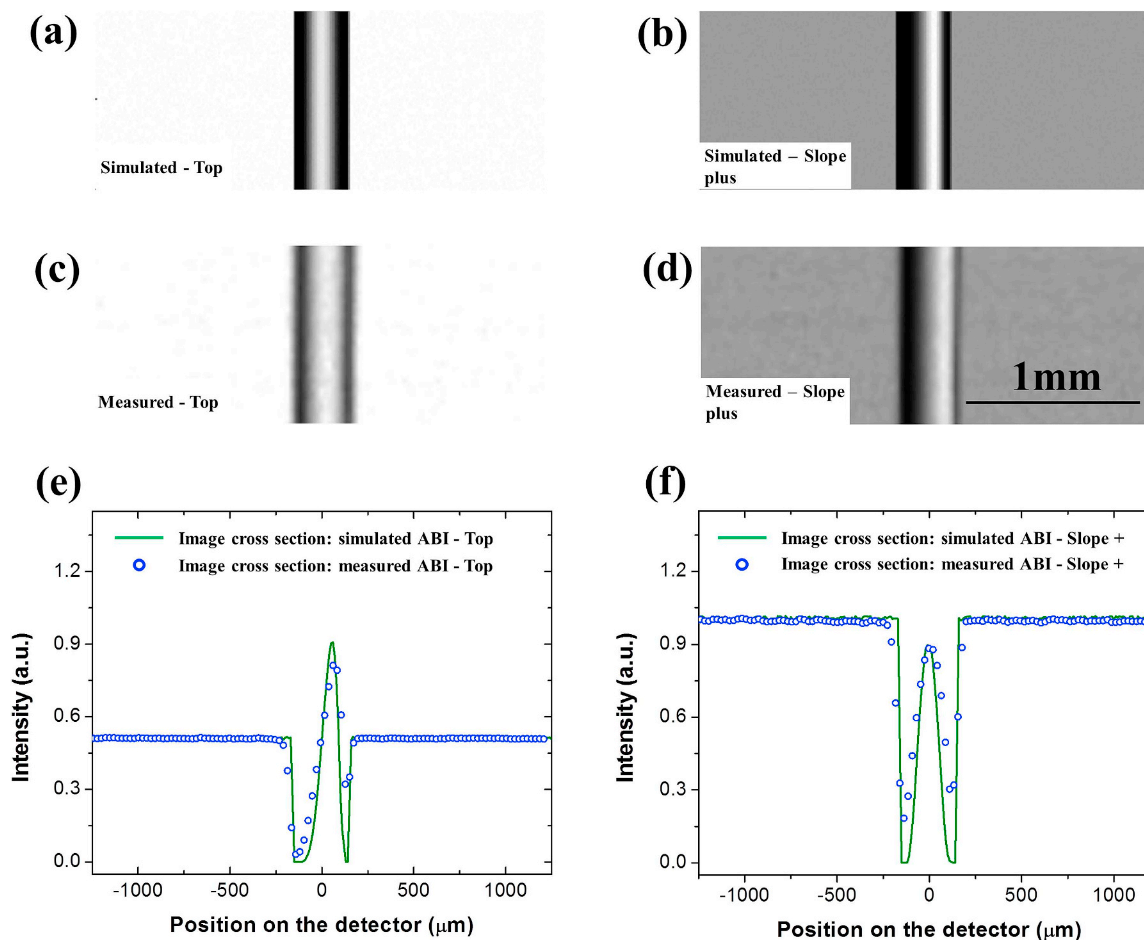

Fig. 8. Experimental validation for a non-dispersive double crystal setup and Si 333 analyzer crystal at 10.7 keV. (a–b) Top and slope plus simulated analyzer-based X-ray phase contrast images (ABI) ($1/\sigma_e$ variable) of a 300 μm thick polyamide wire. (c–d) Top and slope plus measured images. (e–f) Image cross sections. Solid green lines: simulated ABIs. Open blue circles: measured ABIs. (For interpretation of the references to colour in this figure legend, the reader is referred to the Web version of this article.)

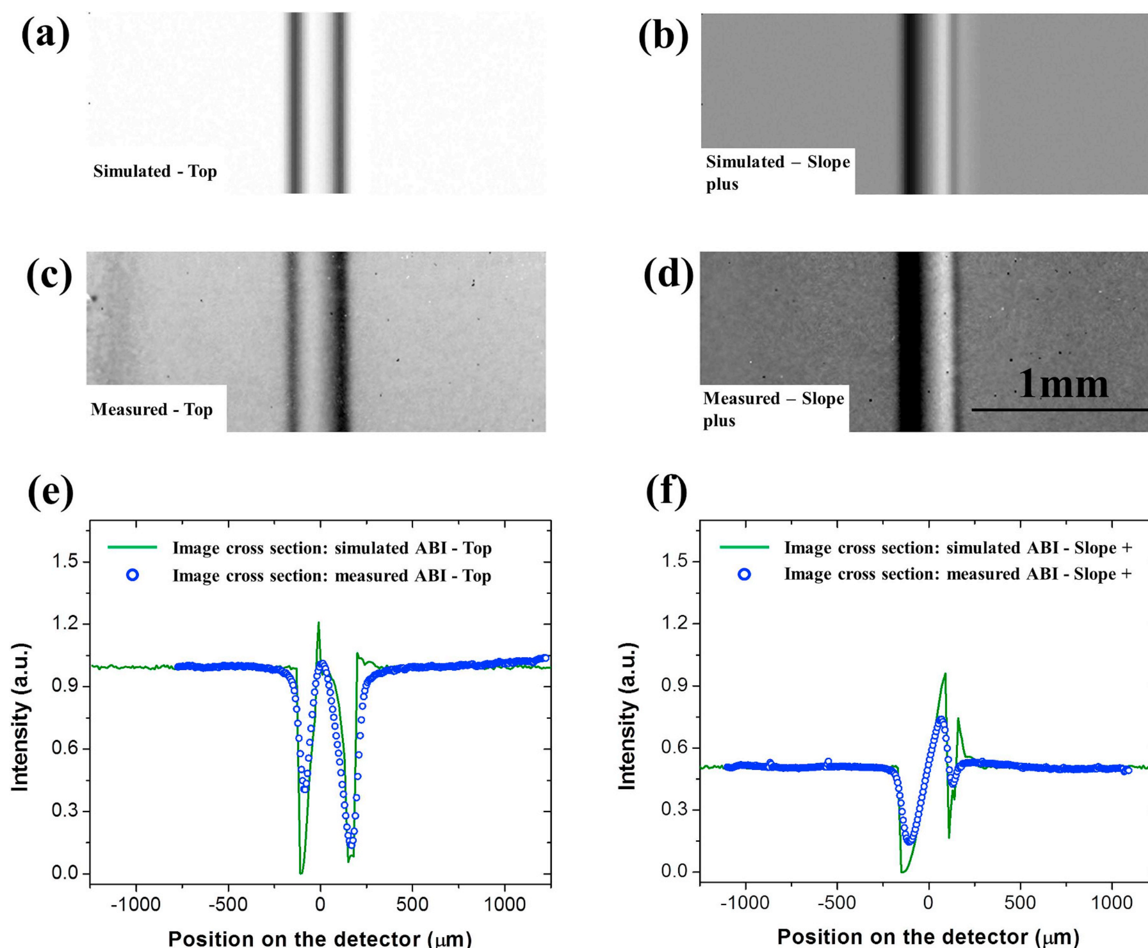

Fig. 9. Experimental validation for a non-dispersive double crystal setup and Si 444 analyzer crystal at 18 keV. (a–b) Top and slope plus simulated analyzer-based X-ray phase contrast images (ABI) ($1/\sigma_e$ variable) of a 300 μm thick polyamide wire. (c–d) Top and slope plus measured images. (e–f) Image cross sections. Solid green lines: simulated ABIs. Open blue circles: measured ABIs. (For interpretation of the references to colour in this figure legend, the reader is referred to the Web version of this article.)

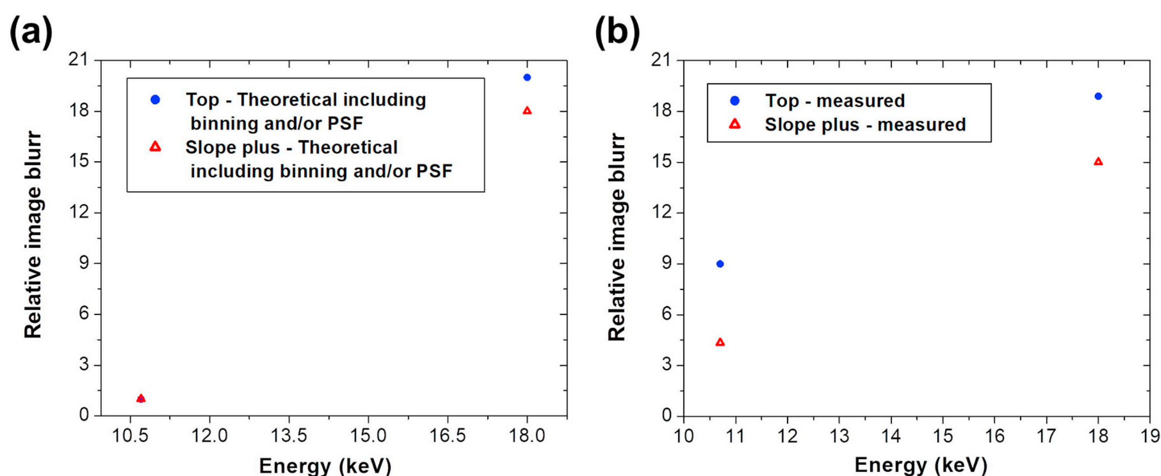

Fig. 10. Relative image blur (RIB) versus X-ray beam energy for experiment validation purposes. (a) Calculated RIB for the non-dispersive double crystal setup for two different energy values (10.7 keV and Si 333 and 18 keV and Si444) including the detector binning and/or the detector point spread function (PSF) for two different angular positions on the analyzer crystal (top and slope plus, which correspond to 1 and 3, respectively in Fig. 4a). (b) Experimental RIB for the same parameters described in (a). The RIBs were determined across the left sample edge.

the detector contribution and the measured images joined with their image cross sections are shown in Fig. 9 for two different angular positions on the analyzer crystal (top and slope plus, which correspond to positions 1 and 3, respectively in Fig. 4a).

The results for both energies (lower and higher) are reasonable, showing that our theoretical model is consistent. However, there are some slight differences between the simulated and measured images for the 10.7 keV ABI non-dispersive double crystal setup which can be

attributed to the narrower theoretical diffraction profile compared with the measured one. This can be easily adjusted. Other slight differences were found for the 18 keV ABI non-dispersive double crystal setup. For Fig. 9e seems that the measured image was not acquired exactly in the top of the analyzer crystal rocking curve. For that the simulation can also be easily adjusted. Another point are the peaks found in the middle of Fig. 9e and in the right side of Fig. 9f. These peaks appeared in the simulated images and are correlated to the singularity in the extinction depth for the maximum value. However, note that for the image 9f there is a very slight tendency on the measured image to follow such a peak. We need to test our model with other image models in order to check if such peaks can be found. Since the singularity point is strongly sensible to stress due strain in the crystal, this value can easily be reduced by a factor of 5. Also for this specific point the divergence of the beam can play an important role, since the width of the $1/\sigma_e$ is angularly narrow at this position. The implementation of the divergence in our code is envisaged.

To be more quantitative, we calculated the RIB for the simulated ABIs including the detector contribution as well as for the measured ABIs. The results are shown in Fig. 10. Significant differences were found in the lower energies ABIs which, as mentioned in the previous paragraph, can be can be attributed to the narrower theoretical diffraction profile compared with the measured one.

5. Discussion and conclusion

We have modeled a dynamical diffraction based X-ray imaging experiment taking into account the variable extinction depth ($1/\sigma_e$). By the simulations we have shown, for an analyzer-based X-ray phase contrast imaging setup (ABI) and a plane and monochromatic X-ray wave beam, that such dynamical diffraction property can severely blur the acquired images, especially at higher energies (18 keV). A more realistic simulation, based on a non-dispersive double crystal setup, including image detector contributions showed close agreement between the simulated and measured images for two different ABI non-dispersive setups (Si 333 double crystal setup at 10.7 keV and Si 444 double crystal setup at 18 keV). Slight differences between the simulated and measured image cross sections were be attributed to: i) narrower theoretical diffraction profile compared with the measured one; ii) slight difference between the theoretical and measured rocking curve angular where the image was acquire and; iii) the singularity in the extinction depth for the maximum value ($1/\sigma_e$) which is responsible for small peaks in the higher energies (18 keV) ABIs. Since the singularity in extinction depth is strongly sensible to stress due strain in the crystal, this effect can easily suppressed in experimental results. Also, for this specific angular position the divergence of the beam can play an important role, since the width of the $1/\sigma_e$ is angularly narrow at this position. The implementation of the divergence in our code, to better estimate this, is envisaged.

Acknowledgements

The authors acknowledge J Manica for the text revision. MG Hönnicke gratefully acknowledges Pró-reitoria de Pesquisa de Pós-graduação (PRPPG) da Universidade Federal da Integração Latino-Americana (UNILA), Brazil (EDITAL PRPPG no. 58/2018) for the financial support.

References

Authier, A., 2001. Dynamical Theory of X-Ray Diffraction. Oxford University Press, New York.

Bravin, A., Mocela, V., Coan, P., Astolfo, A., Ferrero, C., 2007. A numerical wave-optical approach for the simulation of analyzer-based x-ray imaging. Optic Express 15, 5461–5467. https://doi.org/10.1364/OE.15.005641.

Caudevilla, O., Zhou, W., Stoupin, S., Verman, B., Brankov, J.G., 2017. Simulation of a compact analyzer-based imaging system with a regular x-ray source. In: Proc. SPIE 10132, Medical Imaging 2017: Physics of Medical Imaging, pp. 101321P. https://doi.org/10.1117/12.2254500.

Davis, T.J., Gao, D., Gureyev, T.E., Stevenson, A.W., Wilkins, S.W., 1995. Phase-contrast imaging of weakly absorbing materials using hard X-rays. Nature 373, 595–598. https://doi.org/10.1038/373595a0.

Davies, T.J., 1996. Analyzer-based phase contrast imaging and phase retrieval using a rotating anode x-ray source. J. X Ray Sci. Technol. 6, 317–342. https://doi.org/10.1063/1.2825426.

Hönnicke, M.G., Cusatis, C., 2005. X-ray diffraction imaging self-detected with a CCD. J. Phys. D Appl. Phys. 38, A73–A77. https://doi.org/10.1088/0022-3727/38/10A/014.

Hönnicke, M.G., Rigon, L., Arfelli, F., Menk, R.-H., Cusatis, C., 2007. Analyzer-based X-ray phase contrast imaging with four bounce Si(444) monochromators at ELETTRA. Phys. Status Solidi 204, 2740–2745. https://doi.org/10.1002/pssa.200675674.

Hönnicke, M.G., Cusatis, C., de Camargo, P.C., 2008a. Bulk strains in Si induced by thickness mode ultrasonic waves and analysed with x-ray Bragg diffraction. J. Phys. D Appl. Phys. 41, 065401. https://doi.org/10.1088/0022-3727/41/6/065401.

Hönnicke, M.G., Cusatis, C., Antunes, A., Safatle, A.M.V., Barros, P.S.M., Morelhao, S.L., 2008b. Multiple imaging radiography at LNLS. Nucl. Instrum. Methods A 584, 418–423. https://doi.org/10.1016/j.nima.2007.10.036.

Hönnicke, M.G., Manica, J., Mazzaro, I., Cusatis, C., Huang, X.-R., 2012. Source effects in analyzer-based X-ray phase contrast imaging with conventional sources. Rev. Sci. Instrum. 83, 113702. https://doi.org/10.1063/1.4767243.

Hu, W., Huang, X., Yan, H., 2018. Dynamic diffraction artefacts in Bragg coherent diffractive imaging. J. Appl. Crystallogr. 51, 167–174. https://doi.org/10.1107/S1600576718000274.

Johnson, G., King, A., Hönnicke, M.G., Marrow, J., Ludwig, W., 2008. X-ray diffraction contrast tomography: a novel technique for three-dimensional grain mapping of polycrystals. II. The combined case. J. Appl. Crystallogr. 41, 310–318. https://doi.org/10.1107/S0021889808001726.

Kaganer, V.M., Jenichen, B., Ploog, K.H., 2001. Crystal optics elements in a coherent x-ray scattering experiment. J. Phys. D Appl. Phys. 34, 645–659. https://doi.org/10.1088/0022-3727/34/4/327.

Kitchen, M.J., Pavlov, K.M., Siu, K.K.W., Menk, R.H., Tromba, G., Lewis, R.A., 2007. Analyser-based phase contrast image reconstruction using geometrical optics. Phys. Med. Biol. 52, 4171–4187. https://doi.org/10.1088/0031-9155/52/14/010.

Ludwig, W., Cloetens, P., Härtwig, J., Baruchel, J., Hamelin, B., Bastie, P., 2001. Three-dimensional imaging of crystal defects by topo-tomography. J. Appl. Crystallogr. 34, 602–607. https://doi.org/10.1107/S002188980101086X.

Majidi, K., Li, J., Muehleman, C., Brankov, J.G., 2014. Noise and analyzer-crystal angular position analysis for analyzer-based phase-contrast imaging. Phys. Med. Biol. 59, 1877–1897. https://doi.org/10.1088/0031-9155/59/8/1877.

Maksimenko, A., 2007. Nonlinear extension of the x-ray diffraction enhanced imaging. Appl. Phys. Lett. 90, 154106. https://doi.org/10.1063/1.2721378.

Morelhao, S.L., Coelho, P.G., Hönnicke, M.G., 2010. Synchrotron X-ray imaging via ultra-small-angle scattering: principles of quantitative analysis and application in studying bone integration to synthetic grafting materials. Eur. Biophys. J. 39, 861–865. https://doi.org/10.1007/s00249-009-0541-y.

Nesterets, YaI., Gureyev, T.E., Paganin, D., Pavlov, K.M., Wilkins, S.W., 2004. Quantitative diffraction-enhanced x-ray imaging of weak objects. J. Phys. D Appl. Phys. 37, 1262–1274. https://doi.org/10.1088/0022-3727/37/8/016.

Pinsker, Z.G., 1978. Dynamical Scattering of X-Rays in Crystals. Springer, Berlin.

Shabalin, A.G., Yefanov, O.M., Nosik, V.L., Bushuev, V.A., Vartanyants, I.A., 2017. Dynamical effects in Bragg coherent x-ray diffraction imaging of finite crystals. Phys. Rev. B 96, 064111. https://doi.org/10.1103/PhysRevB.96.064111.

Tanner, B.K., 1976. X-ray Diffraction Topography. Pergamon, Oxford.

Zhang, H., Chapman, D., Zhong, Z., Parham, C., Gupta, M., 2007. Crystal tilt error and its correction in diffraction enhanced imaging system. Nucl. Instrum. Methods A 572, 961–970. https://doi.org/10.1016/j.nima.2006.12.019.

Zhou, W., Majidi, K., Brankov, J.G., 2014. Analyzer-based phase-contrast imaging using micro focus X-ray source. Rev. Sci. Instrum. 85, 085114. https://doi.org/10.1063/1.4890281.